

Article

Adsorption of Ciprofloxacin and Lidocaine by Non-Fibrous Raw Mg-Clays: The Role of Composition and Texture

Maria Eugenia Roca-Jalil ^{1,2,*}, Telma Musso ^{2,3}, Vanina Rodriguez-Amejjide ^{1,2}, Micaela Sanchez ^{1,2}, Andrea Maggio ^{1,2}, Miria Teresita Baschini ^{1,2} , Gisela Pettinari ^{2,3}, Luis Villa ⁴, Manuel Pozo ^{5,*}  and Alejandro Pérez-Abad ⁴

- ¹ Institute of Research and Development in Process Engineering, Biotechnology, and Alternative Energies (PROBIEN, CONICET-UNCo), Neuquén 8300, Argentina; vanina.rodriguez@fain.uncoma.edu.ar (V.R.-A.); micaela.sanchez@fain.uncoma.edu.ar (M.S.); andrea.maggio@probien.gob.ar (A.M.); miria.baschini@fain.uncoma.edu.ar (M.T.B.)
- ² Department of Chemistry, Faculty of Engineering, National University of Comahue, Neuquén 8300, Argentina; telma.musso@probien.gob.ar (T.M.); gisela.pettinari@probien.gob.ar (G.P.)
- ³ Department of Geology and Petroleum, Faculty of Engineering, National University of Comahue, Neuquén 8300, Argentina
- ⁴ Minersa Group, 48992 Getxo, Spain; luis.villa@minersa.com (L.V.); alejandro.perez@minersa.com (A.P.-A.)
- ⁵ Department of Geology and Geochemistry, Faculty of Sciences, Cantoblanco Campus, Autonomous University of Madrid, 28049 Madrid, Spain
- * Correspondence: eugenia.rocajalil@probien.gob.ar (M.E.R.-J.); manuel.pozo@uam.es (M.P.); Tel./Fax: +54-2994490688 (M.E.R.-J.); +34-660050721 (M.P.)

Abstract: This study evaluated non-fibrous Mg-clays as potential adsorbents of emerging contaminants (ECs) from water. The materials were characterized, and their textural and structural properties were related to their ability to remove two model EC molecules: ciprofloxacin (CPX) and lidocaine (LID). The results showed that Ad-6 and Ad-7 are mixed-layer kerolite/stevensite, while Ad-5 and Ad-8 are mainly composed of smectite minerals like stevensite and saponite, respectively. Ad-8 exhibited the highest CPX-adsorption capacity (0.91 mmol·g⁻¹ clay), likely due to its saponite content. Mixed-layer materials also performed well, with Ad-6 and Ad-7 achieving an adsorption capacity of 0.8 and 0.55 mmol·g⁻¹ clay, respectively. Adsorption studies suggested that CPX is adsorbed through ion exchange in materials with high smectite content (Ad-8 and Ad-5), while interstratified materials showed enhanced retention due to kerolite presence, which improves their porous structures. Similar findings were observed for LID, indicating a cationic-exchange mechanism for LID adsorption in all the materials and suggesting that the molecular size of the EC could regulate the removal capacity of these materials. This work showed that the studied Mg-clays could be effectively used for the removal of pharmaceutical pollutants, expanding their commercial possibilities.

Keywords: Mg-clays; emerging contaminants; removal from water; adsorption



Citation: Roca-Jalil, M.E.; Musso, T.; Rodriguez-Amejjide, V.; Sanchez, M.; Maggio, A.; Baschini, M.T.; Pettinari, G.; Villa, L.; Pozo, M.; Pérez-Abad, A. Adsorption of Ciprofloxacin and Lidocaine by Non-Fibrous Raw Mg-Clays: The Role of Composition and Texture. *Minerals* **2024**, *14*, 966. <https://doi.org/10.3390/min14100966>

Academic Editors: Jianxi Zhu, Teresa Pereira da Silva, Daniel P. S. De Oliveira and João Pedro Veiga

Received: 6 August 2024

Revised: 13 September 2024

Accepted: 21 September 2024

Published: 25 September 2024



Copyright: © 2024 by the authors. Licensee MDPI, Basel, Switzerland. This article is an open access article distributed under the terms and conditions of the Creative Commons Attribution (CC BY) license (<https://creativecommons.org/licenses/by/4.0/>).

1. Introduction

The large production of medicines worldwide (around 4000 types in the order of 200,000 tons per year) is a major cause of the progressive increase in pharmaceutical contaminants that are released to the environment with undervalued consequences on ecosystems and water quality [1–6]. The greatest concern of releasing antibiotics to aquatic environments, either directly or indirectly by surface runoff or soil leaching, is related to the evolution of antimicrobial resistance genes and antimicrobial-resistant bacteria, which reduces the therapeutic potential against human and animal pathogens [7–10].

Ciprofloxacin (CPX) and lidocaine (LID) are considered contaminants of emerging concern due to their presence in wastewater effluents, surface waters, and groundwaters [6,8,11]. CPX is one of the most widely used antibiotics in human health [12,13]. This compound is highly soluble in water (about 1.35 mg·mL⁻¹) under different pH conditions and highly stable in

wastewater and soil [14]. Meanwhile, lidocaine is a topical local anesthetic of the amide type with immediate onset of action. Both humans and animals metabolize LID to various metabolites. Its n-octanol/water partition coefficients indicate a tendency to remain in the water phase instead of accumulating in sewage sludge or in aquatic organisms [1,11,15].

Several methods have been put in place for the sequestration of pharmaceutical pollutants from their aqueous environment. Conventional methods like lime softening, reverse osmosis, distillation, and sedimentation were determined to be not efficient in removing antibiotics from wastewater completely [16–18]. Other methods different from conventional procedures, like membrane separation, electrodialysis, ozonation, and advanced oxidation processes, were also evaluated [19]. However, some of these methods produce toxic by-products, which are even more harmful than the original contaminants [20]. Compared to other remediation methods, adsorption has several benefits, such as simplicity, reliability, low energy requirement, and easy recovery of the adsorbent [21]. The two types of adsorptive processes used for the removal of antibiotics from water or wastewater are the Batch process and the Continuous process, either of which can be utilized using different adsorbents like Activated Carbons, Biochars, clay minerals, Carbon Nanotubes, ion-exchange resins, and Zeolites [20].

Clay minerals occur as large deposits worldwide, which guarantees their continuing abundance and availability for numerous applications due to their relatively low cost. These phyllosilicates differ in the arrangement of the tetrahedral and octahedral sheets and the distribution of surface electric charge. They exhibit special properties such as high adsorption, ion-exchange capability, or swelling behavior, resulting from their nonpareil structure, the presence of surface OH groups, and weak electrostatic interactions between layers and/or sheets and the exchangeable cations [22,23].

Several types of clay minerals, such as montmorillonite [24], halloysite [25], kaolinites [26], sepiolite [27], and palygorskite [28], have been investigated for the removal of pollutants in aqueous media. Particularly, montmorillonite-rich bentonites have proven to be effective adsorbents for a variety of drugs, such as antibiotics, anti-inflammatories, and anesthetics, among others [29–31]. Also, in the search for adsorbent materials that are both natural and versatile in retaining such molecules or their analytes, alternative clay minerals have gained attention [27,32–39].

The magnesian clays consist of mostly 2:1 clay minerals that are differentiated as non-fibrous clay minerals (kerolite, stevensite, and saponite) and fibrous clay minerals (sepiolite and palygorskite). Saponite and palygorskite contain more aluminum than stevensite, kerolite, and sepiolite. Kerolite (turbostratic talc for the IMA), Mg-smectite, and sepiolite form a clay assemblage found in Neogene continental deposits of the Madrid Basin (Spain) that originated in saline-alkaline lacustrine–palustrine environments [40,41]. Kerolite-Mg-smectite clays from the Madrid Basin deposits show exceptional suitability as adsorbent material in biotechnology processes, including as adsorbent for mycotoxins [42,43]. Moreover, pesticide removal from water has also been observed [44]. Bentonites from the Madrid Basin are characterized by the fact that they consist of magnesian smectites, mainly saponite. These bentonites have a large number of applications, which mainly include pet litter, drilling muds, and foundry sands, but also as oil and grease absorbents, agricultural pesticide carriers, and clarifying and decolorizing agents [45].

Adsorption studies on stevensite for the removal of different types of contaminants from water, such as heavy metals, methyl violet, and tetracycline, have been reported [39,46,47]. Kerolite has been tested for removing pesticides and herbicides from an aqueous solution [44,48,49]. Saponite has been evaluated in photocatalytic and adsorption processes for water treatment [38].

Several references can be found on CPX adsorption on natural and modified clays such as bentonite, kaolinite, or pillared clay [14,29,30,50–52]. However, neither CPX nor LID adsorption on Mg-clays has been documented. Unlike smectite, the surface characteristics of non-fibrous Mg-clays remain underexplored for its potential application in environmental remediation. Thus, the aim of this work was to evaluate four non-fibrous Mg-clays as novel

materials for the removal of ciprofloxacin and lidocaine compounds, which are considered emerging contaminants. Their adsorptive behavior was explained on the basis of their composition and textural properties. In this way, promising clay materials are presented for the removal of pharmaceutical pollutants.

2. Materials and Methods

2.1. Raw Mg-Clays

Four samples of raw Mg-clays (Ad-5, Ad-6, Ad-7, and Ad-8) of industrial interest were selected from the Esquivias–Batallones quarries located in the Madrid basin Neogene deposits [53]. Hand specimen observations are described below. Ad-5: compacted claystone, with intraclastic morphologies of different sizes enclosed by cementing clay. It shows some morphologies with concentric structures and burrower fillings. The large number of small circular pores (<0.2 mm) is noteworthy. Predominantly greenish in color, although locally pinkish tones are observed (5GY 6/1). Ad-6: clay-clast intrarenite of moderate compactness, massive, and with evidence of burrowing activity and small perforations with fillings. Staining of black Mn-Fe oxides and waxy films on surfaces. Pinkish gray in color (5YR 8/1). Ad-7: clay-clast intrarenite, consisting of crumbly granular morphologies with local cementing clayey material and abundant pore roots. Pinkish gray in color (5YR 8/1). Ad-8: compacted and massive claystone, showing slickensides with striations and staining of black Mn-Fe oxides. It presents a yellowish-green color (5Y 7/2).

Structural and Physicochemical Characterization of Raw Mg-Clays

The four samples were subjected to mineralogical analysis by means of X-ray diffraction (XRD) in a Bruker D8 with Lynxeye XE-T detector equipment (Bruker, Billerica, MA, USA) using $\text{CuK}\alpha$ radiation (40 kV, 20 mA) and a scanning speed of $1^\circ 2\theta/\text{min}$. The powdered whole-rock samples were used to determine bulk mineralogy. After clay fraction separation (<2 μm), sample mounts were prepared from suspensions oriented on glass slides. The identification of clay minerals was carried out on the samples air-dried (AD), with ethylene glycol solvation (EG), and heated at 550 $^\circ\text{C}$. The mineral intensity factors (MIF) method was applied to XRD reflection intensity ratios normalized to 100% with calibration constants for the quantitative estimation of mineral content [54]. In the mixed-layer samples formed by mixed-layers, X-ray diagrams modeled using the NEWMOD program were used as a reference [40,41].

The thermal analyses (DSC/DTA/TGA Q600 of TA Instruments) (TA Instruments, Inc., New Castle, DE, USA) of the samples were performed using 10 mg of powdered clay sample in a Pt sample holder at an average heating rate of 10 $^\circ\text{C}/\text{min}$ with an alumina reference. The infrared spectroscopy (FTIR) (Bruker IFS 66v standard) (Bruker, Billerica, MA, USA) spectra were recorded with a spectral resolution of 2 cm^{-1} in transmission mode in the region of 400–4000 cm^{-1} . The samples were examined in KBr pellets (3 mg:300 mg^{-1} KBr). Samples were examined under scanning electron microscopy (SEM) using an S-3000N microscope with an ESED detector (Hitachi, Chiyoda, Japan) attached to an Oxford Instruments EDX analyzer (Oxford Instruments, Abingdon, UK), model ICAX-sight. The surface of the fractured sample was coated with a 10 nm gold film.

Chemical analyses were carried out using sample fusion and inductively coupled plasma atomic emission spectroscopy (ICP-AES) at the ACTLABS laboratory (Canada). The detection limits for analyses were between 0.01 and 0.001 wt.% for major elements.

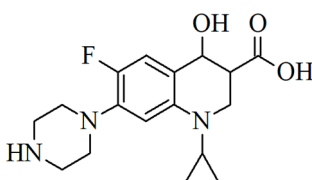
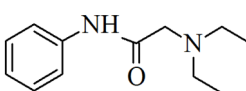
Cation-exchange capacity (CEC) was measured using the copper triethylenetetramine $[\text{Cu}(\text{trien})]^{2+}$ method [55]. Textural properties were studied by nitrogen adsorption-desorption isotherms at -196.15°C . These were measured using a Micromeritics ASAP2020 manometer (Micromeritics Instrument., Norcross, GA, USA) on degassed samples at 200 $^\circ\text{C}$ for 12 h. The apparent specific surface area was calculated by the Brunauer, Emmet, and Teller (S_{BET}) method. Micropore volume (V_{mp}) was calculated by applying the α -plot method [56]. The total pore volume (V_{T}) was calculated by applying Gurvich's rule at a relative pressure of 0.98, and the mesopore volume (V_{mp}) was calculated by using of

BJH method [57]. Pore classification used was the one proposed by IUPAC [57], which states that pores whose size exceeds 50 nm are macropores, pores whose size is between 2 and 50 nm are considered mesopores, and pores whose size is less than 2 nm are called micropores. The water vapor isotherms were obtained at 20 °C using the technique described by [30]. Hydrophilicity and water adsorption capacity were estimated from these isotherms. Natural humidity content (NH) was obtained by calculating the difference between the initial mass of the natural sample and its mass at 0% relative humidity. The amount of water adsorbed at relative humidity (RH) values (15%–20%) was also calculated. This value correlates well with the monolayer coverage on the surface of clay minerals and allows determining the amount of adsorbed water measured in $\text{mmol}\cdot\text{g}^{-1}$ (q_{ads}) and the monolayer surface area (S) in samples at 16.3% RH samples to be determined [58,59].

2.2. Adsorbates

The organic molecules selected as models were an anesthetic (LID) and an antibiotic (CPX), two pharmaceutical compounds with a high environmental impact. The CPX is usually used as ciprofloxacin hydrochloride (CPX.HCl), but its molecule exhibits a nearly planar structure, lacks chiral carbons, and, therefore, does not display optical isomerism. Nevertheless, the presence of protonable carboxyl, carbonyl, and amino groups in its structure imparts amphoteric behavior, leading to the formation of different species depending on the physical state or pH of the solution in which it is present [60]. Physically, it is a white crystalline solid with a melting point of 75 °C, exhibiting high stability under various pH values and temperature conditions [61]. LID can exist as a lidocaine base, meaning it is neutral and therefore insoluble in water, or its more soluble form as lidocaine monohydrate hydrochloride (LID.HCl.H₂O) [62]. Chemically, the LID molecule features an amide group and an amino group; the latter can be protonated–deprotonated, depending on the pH of the contacting medium, leading to the generation of different species in solution [63]. The structural and chemical properties of CPX and LID are shown in Table 1.

Table 1. General characteristics of organic molecules studied.

	Ciprofloxacin	Lidocaine
Structure		
Chemical formula	C ₁₇ H ₁₈ FN ₃ O ₃	C ₁₄ H ₂₂ N ₂ O
Molecular weight (g.mol ⁻¹)	331.45	288.80
Molecular dimensions (nm)	1.30 × 0.30 × 0.70 [60]	1.04 × 0.60 × 0.59 *
pKa	pKa ₁ = 5.90; pKa ₂ = 8.90	pKa = 7.92

* The dimensions of the molecule were calculated by using Avogadro software (1.1.1 version, 2013).

2.3. Adsorption Experimental Procedure

CPX and LID were employed in their hydrochloride forms as adsorbates. CPX.HCl, sourced from Magel S.A., and LID.HCl.H₂O, obtained from Parafarm (Parapharm Pharmaceuticals Group, Athens, Greece), were used, both with a purity of 99.9%. Adsorption studies were conducted under conditions previously reported by the research group for other materials [30,50,51]. All adsorption tests were carried out using 20 mg of adsorbent in contact with a drug solution at a ratio of 2.5 g·L⁻¹. These studies were conducted at 20 °C, without initial pH adjustment (pH values of around 5–6), and in all cases, separation was achieved through centrifugation at 8000 rpm for 20 min using a SOVALL ultracentrifuge (Thermo Fisher Scientific, Waltham, MA, USA).

Initial concentrations of 0.3 mM for CPX and 1.69 mM for LID were used for kinetic studies. Adsorption isotherms were obtained with concentrations ranging from 0.15 to 3 mM for CPX and 0.2 to 5 mM for LID, allowing the system to reach equilibrium over a 24-h contact period, both in accordance with previous works [30,51].

CPX and LID concentrations were quantified using a UV-Vis T60 spectrophotometer at their respective maximum wavelengths, and the adsorbed quantity was calculated by Equation (1).

$$q = \frac{(C_i - C_e) * V}{w} \quad (1)$$

where C_i and C_e are the initial and equilibrium concentrations (mM), V is the solution volume (L), and w is the mass of adsorbent (g).

The experimental data were fitted to the widely used theoretical models of Langmuir, Freundlich, and Sips in order to calculate the maximum adsorption capacity of the samples under the studied conditions.

3. Results and Discussion

3.1. Characterization of Mg-Clays

XRD analyses indicated that samples Ad-6 and Ad-7 showed a high phyllosilicate content ($\geq 98\%$) with traces ($<5\%$) of quartz and potassic feldspars (Figure 1A, Table 2). In the bulk sample, the powder patterns showed a band between 2 and $10^\circ 2\theta$, characteristic of an irregular kerolite/Mg-smectite mixed layer [40,64], which was corroborated by the existence of reflections typical of this material. In particular, the d_{060} reflection at approximately 1.527 Å supports the trioctahedral character of the constituent clay minerals. The study of the clay fraction with different treatments indicated the presence of both a swelling and a non-swelling phase in Ad-6, but almost exclusively non-swelling in Ad-7 (Figure 1B). The use of the NEWMOD program to model the interstratification showed in sample Ad-6 a predominance of Mg-smectite (80%–90%), while in Ad-7, a predominance of kerolite (80%) was observed. These results were coherent with those reported in other papers [40,41].

In sample Ad-5, phyllosilicates are the main constituents (99%), with minor amounts of quartz and potassic feldspar ($<5\%$). In the bulk sample, two reflections at 15 Å and at around 10 Å can be observed. Also, the d_{060} value indicated the presence of trioctahedral clay minerals. Oriented samples showed the presence of a swelling phase (87%) and illite (13%) (Figure 1B).

Sample Ad-8 was also predominantly composed of phyllosilicates at 14–15 Å (96%), with traces ($<5\%$) of quartz and feldspars (both potassic and plagioclase). The d_{060} spacing was predominantly trioctahedral (1.533 Å), although a minor reflection at 1.502 Å was also identified, indicating the presence of dioctahedral phases (Figure 1A). In the clay fraction, predominantly smectite (97%) and a low content of illite (3%) were identified. This material can be considered as a bentonite.

Table 3 shows the chemical composition of the raw Mg-clays. The results were consistent with the mineralogy of the samples. Thus, the kerolite/Mg-smectite mixed layer samples exhibit the highest percentages of MgO and the lowest percentages of Al_2O_3 . The SiO_2/MgO molar ratio is the lowest, between 1.25 and 1.46. MgO content in Ad-5 is also significant, although this clay has a higher Al_2O_3 content than the kerolite/Mg-smectite mixed layer samples. Bentonite has the highest Al_2O_3 content but the lowest MgO content, resulting in a SiO_2/MgO molar ratio of 2.25. The levels of aluminum and titanium in Ad-5 and Ad-8 correspond to the illite phase, which is absent in the other samples.

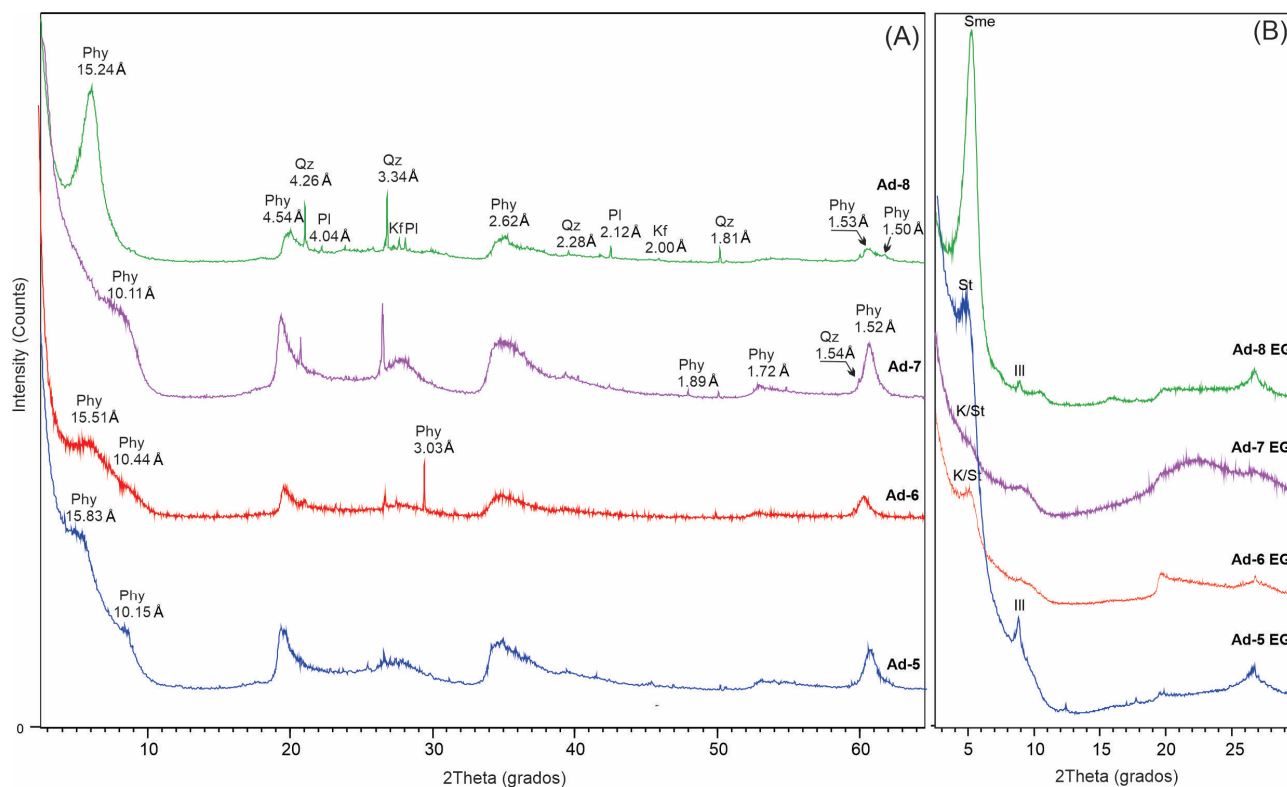


Figure 1. Powder X-ray patterns of the Mg-clays: (A) X-ray patterns of <2 μm grain size fractions, oriented ethylene glycol solvated samples (B) Phyl: phyllosilicates; Sme: smectite; Qz: quartz; Kf: potassium feldspar; Pl: plagioclase; K/St: kerolite–stevensite mixed layer. St: stevensite; Ill: illite.

Table 2. Bulk (% w/w) and clay mineralogy (% w/w) of the Mg-clays determined by XRD. Phyl: phyllosilicates, Qz; quartz; Kf: potassium feldspar; Pl: plagioclase; Sme: smectite; K/St kerolite–stevensite mixed layer; Ill: illite. Tr: trace.

Samples	Bulk Mineralogy				Clay Fraction		
	Phyl	Qz	Kf	Pl	Sme	Ill	K/St
Ad-5	99	<1	<1	-	87	13	-
Ad-6	99	1	Tr	-	-	-	K ₂₀ St ₈₀
Ad-7	98	2	-	-	-	-	K ₈₀ St ₂₀
Ad-8	96	2	1	1	97	3	-

Table 3. Major element chemistry of studied non-fibrous Mg-clays.

Chemical Analysis (%)	Ad-5	Ad-6	Ad-7	Ad-8
SiO ₂	50.15	51.43	53.17	48.23
Al ₂ O ₃	4.96	2.54	1.27	9.37
Fe ₂ O ₃	1.92	0.63	0.46	3.03
MnO	0.025	0.013	0.006	0.045
MgO	23.09	24.79	27.09	14.37
CaO	0.54	0.96	0.38	0.87
Na ₂ O	0.09	0.08	0.06	0.22
K ₂ O	0.91	0.6	0.34	1.11
TiO ₂	0.233	0.115	0.058	0.363
P ₂ O ₅	0.08	0.03	<0.01	0.07
LOI	18.15	17.34	16.09	20.57

These results, together with the test conducted [65] to differentiate between the different magnesian smectites, allowed us to identify a predominance of stevensite in sample

Ad-5 and in the kerolite/Mg-smectite mixed layer, while the composition of the Mg-smectite present in the bentonite is a saponite.

The infrared spectra of the samples formed by stevensite and kerolite/stevensite mixed layer encompassed a broad band in the range of 3000–3400 cm^{-1} with maximum absorption at 3451 cm^{-1} , presenting a small shoulder at a somewhat higher frequency corresponding to the OH-stretching bands of adsorbed and interlamellar water, respectively (Figure 2). The presence of an absorption band at 3677 cm^{-1} is characteristic of trioctahedral minerals and corresponds to the OH-Mg-Mg stretching band [66]. At lower frequencies, an intense absorption band at 1019 cm^{-1} is typical of silicates (Si-O stretching band), while the band at 667 cm^{-1} confirms the presence of trioctahedral minerals, as it corresponds to the Si-O-Mg deformation band (Figure 2). The presence of quartz was observed in all samples (around 784 cm^{-1}), which is in line with the XRD results.

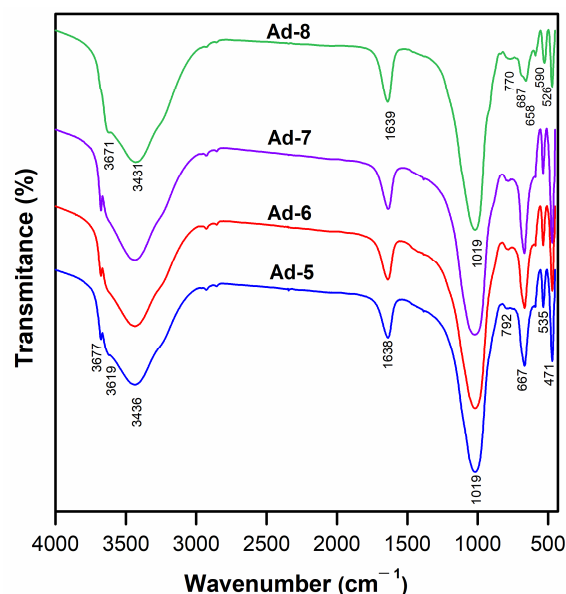


Figure 2. FT-IR spectra of the bulk samples of Mg-clays. Wavenumber peaks are indicated.

The infrared spectrum of the bentonite sample was very similar to that of the stevensite and kerolite/stevensite mixed-layer samples. Between 2000 and 4000 cm^{-1} , the large absorption band at 3428 cm^{-1} in Ad-8 coincides with that present between 3431 and 3434 cm^{-1} in the other samples (Figure 2) [66]. The presence of the effect at 3617 cm^{-1} was indicative of the presence of Al in the octahedral layer. Between 2000 and 450 cm^{-1} , the absorption bands around 1636 cm^{-1} and the intense one at 1017 cm^{-1} coincide, as well as those at 667 cm^{-1} and 469–470 cm^{-1} . A small absorption peak at 590 cm^{-1} and the existence of a small band at 658 cm^{-1} with a shoulder at 687 cm^{-1} stood out in Ad-8, which contrasts with a better-defined peak at 667 cm^{-1} in the other samples (Figure 2).

From the point of view of thermal behavior (Figure 3), the samples formed by the stevensite and kerolite/stevensite mixed layer behaved similarly. The first endothermic peak was observed at low temperatures (66–74 $^{\circ}\text{C}$), which is attributed to the loss of zeolitic water: water adsorbed on the surface and hydration of the exchange cations [67]. The second endothermic peak at high temperatures (803–810 $^{\circ}\text{C}$) can be attributed to dehydroxylation followed by an exothermic peak (828–830 $^{\circ}\text{C}$) due to the formation of a high-temperature phase. The total weight loss of the samples had a variation between 15 and 20%, with the sample with the highest loss featuring a mineralogy with a predominance of stevensite (Ad-5).

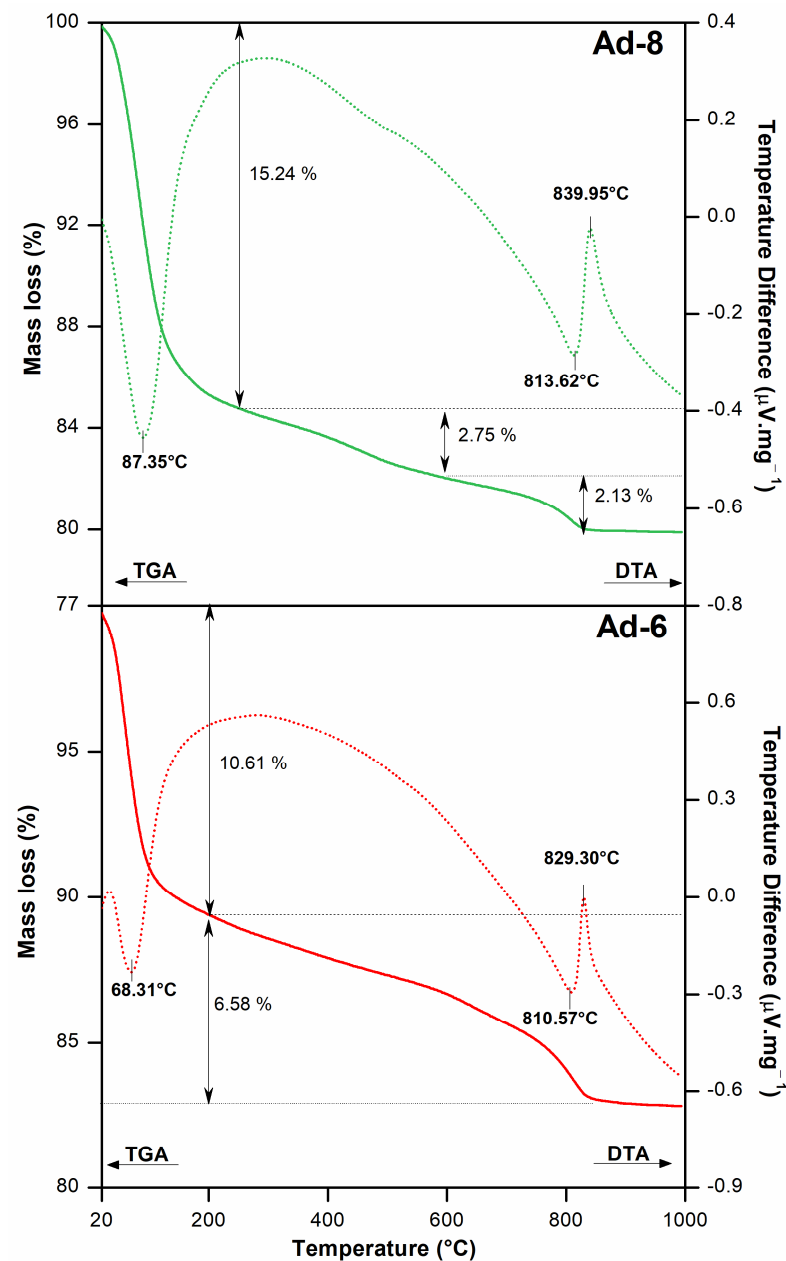


Figure 3. DTA (dotted lines) and TG (full lines) curves of the bentonite (Ad 8) and one representative kerolite/stevensite mixed layer (Ad 6).

The bentonite sample showed three endothermic peaks. One was at a low temperature (<90 °C), which is attributed to dehydration, loss of adsorbed water on external surfaces, and hydration of the exchange cations [67]. Another was at medium temperature (477 °C), assigned to dehydroxylation of the remaining coordination water and hydroxyls or structural water [68]. Finally, at high temperatures (813 °C), a third possibly corresponds to the residual dehydroxylation of the silanol groups [69]. The exothermic peak (828 °C) represents the destruction of the structure and formation of a high-temperature phase [69]. The total weight loss value of the sample is 20%.

The microfabric characteristics of the four Mg-clays studied are described below. The terminology for the microfabric type is that proposed by [70].

Ad-5. Matrix-skeletal microfabric with complex distribution of constituents and different types of porosity. Some morphologies with coatings and scattered mineral grains (Figure 4a). In wrinkled morphologies, there are abundant pores with diameters generally

less than 10 μm . The particle size is small ($<0.5 \mu\text{m}$), and morphological features are characteristic of smectites.

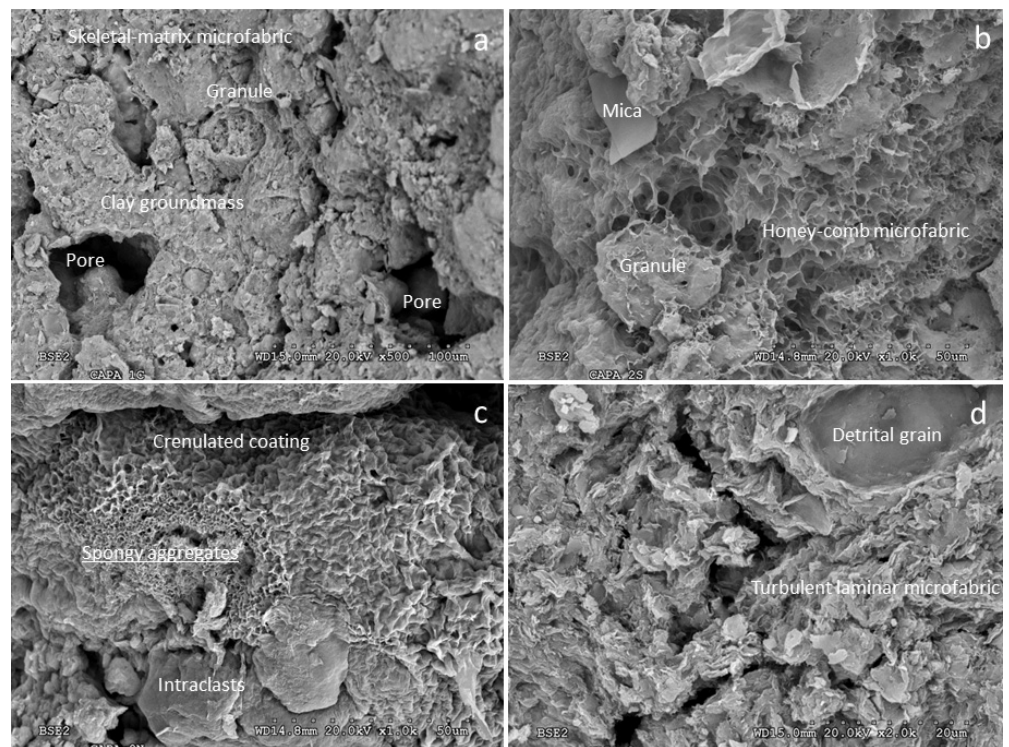


Figure 4. (a) Ad-5. Matrix-skeletal microfabric showing the presence of granules embedded in a clayey mass (matrix) with small pore sizes (up to 80 μm) related to bioturbation. (BSE); (b) Ad-6. Porous coatings on the clayey mass and granules showing a honeycomb microfabric, with some mica grains included. (BSE); (c) Ad-7. Spongy aggregates have been observed coating porosities or enveloping morphologies (granules and intraclasts) with wrinkled shapes on the surface. (BSE); (d) Ad-8. The clay has a turbulent laminar micro-fabric, where the micro-laminae are less than 5 μm thick and may envelop detrital grains. (BSE).

Ad-6. Matrix-skeletal-type microfabric, where granular morphologies of variable size and porous coatings on surfaces can be recognized. Different textural types are identified in the clayey material: one is massive with a clastic appearance, another has a large wrinkled appearance, and a third has smaller wrinkles made up of a very porous microfabric with face-edge and edge-edge (honeycomb) arrangements (Figure 4b). This sample presents laminar morphologies characteristic of smectite with sizes smaller than 2 μm that may be accompanied by sepiolite fibers.

Ad-7. Matrix-skeletal to sponge-like microfacies in areas where dense morphologies, detrital grains, and spongy clay films are recognized. The spongy aggregates show a high porosity of small size. Locally, there are thin clayey films formed by fibrous aggregates coating dense morphologies and spongy aggregates (Figure 4c). The sample presents very small morphologies ($<0.5 \mu\text{m}$) together with other more wrinkled morphologies of larger size.

Ad-8. A matrix-type microfabric, although locally, it may show a turbulent laminar microfabric formed by dense aggregates of lamellar particles that may show incipient fiber growth (Figure 4d). There are laminar morphologies of small size (0.5 μm) forming aggregates, characteristic of smectite. Locally incipient sepiolite fibers are observed.

CEC values were related to the expansible clay mineral content of the analyzed samples. The highest value was found in the bentonite sample (saponite, Ad-8), followed by the sample with a predominance of stevensite (Ad-5) (Table 4). In these two smectitic samples, CEC behavior was in agreement with saponite's higher layer charge with regard to

stevensite. The kerolite/stevensite mixed layer showed values of 38.4 cmol(+).Kg⁻¹ (Ad-7), 48.6 cmol(+).Kg⁻¹ (Ad-6), evidencing a proportional relationship between the stevensite content and the increment in cation-exchange capacity.

Table 4. Physicochemical and textural properties of Mg-clay.

	Ad-5	Ad-6	Ad-7	Ad-8
CEC (cmol(+).Kg ⁻¹)	53	48.6	38.4	90.86
S _{BET} (m ² .g ⁻¹)	240	244	280	203
S _{ext} (m ² .g ⁻¹)	195	201	245	116
V _T (cm ³ .g ⁻¹)	0.24	0.31	0.35	0.17
V _{μp} (cm ³ .g ⁻¹)	0.02	0.02	0.01	0.03
V _{mp} (cm ³ .g ⁻¹)	0.18	0.24	0.31	0.10

Figure 5 shows the N₂ adsorption–desorption isotherms at −196.15 °C. The isotherms were classified as type II according to the IUPAC classification, although the hysteresis cycles exhibit different classifications. Mg-clays Ad-5 and Ad-8 exhibit a type H4 cycle, which is associated with the presence of lamellar particle aggregates, common in smectite clays, whereas Ad-6 and Ad-7 display type II b cycles, characteristic of structures with interconnected pores, some of which are blocked during desorption [57]. This difference can be related to the presence of kerolite, given that its content in the mixed layer structure increased from 20% to 80%. The desorption behavior in samples with kerolite suggests greater pore interconnection. This observation is in agreement with the textural properties shown in Table 4, where these samples are predominantly mesoporous.

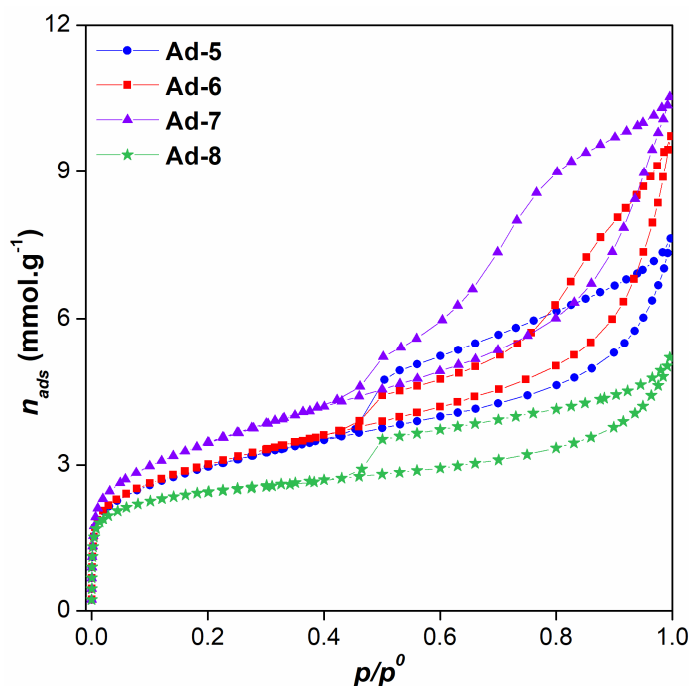


Figure 5. N₂ adsorption–desorption isotherms at −196.15 °C of Mg-clays.

The presence of kerolite appeared to enhance the specific surface area (S_{BET}) and mesoporosity, the latter closely related to the total pore volume. Moreover, the increasing amount of kerolite correlated well with changes in hysteresis loop patterns, suggesting that kerolite promotes interconnectivity within the mesoporous structure of the Mg-clays. The bentonite Ad-8, predominantly made up of trioctahedral smectite of saponite composition, exhibited textural properties typical of such minerals, with hysteresis cycles indicating mesopores accounting for 80% of the total pore volume.

When comparing these results across the four Mg-clays, the specific surface area (S_{BET}) values are notably higher for the kerolite/stevensite mixed layer compared to bentonite. Stevensite sample Ad-5 had an S_{BET} value higher than the saponite but lower than the kerolite/stevensite mixed-layer samples. This difference underscores how the presence of kerolite enhances porosity. The results obtained for S_{BET} values are in line with those previously reported for similar samples [46,71,72].

The water vapor adsorption isotherms are shown in Figure 6, with corresponding parameters detailed in Table 5. All Mg-clays display a water vapor adsorption behavior similar to that observed in swelling clay minerals. At low relative humidity (RH), Ad-7, which contains the highest proportion of kerolite, exhibited the lowest water adsorption. This can be attributed to the limited capacity of kerolite to retain water within its structure, unlike conventional clay minerals.

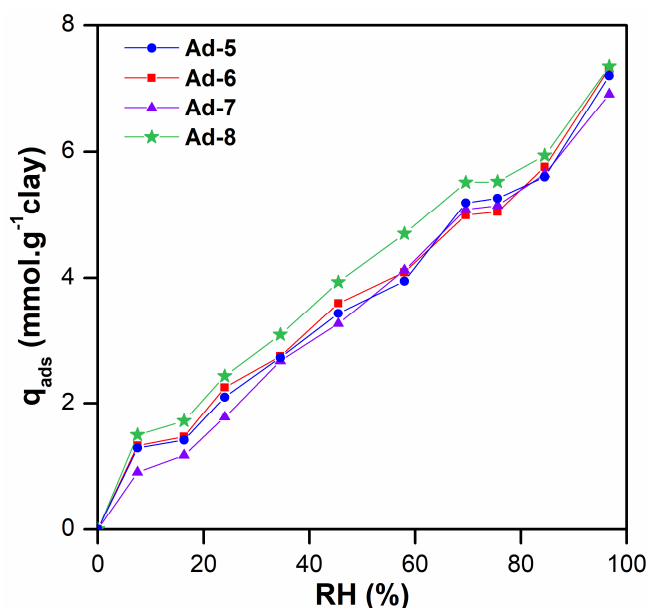


Figure 6. Water adsorption isotherms at 20 °C of Mg-clays.

Table 5. Parameters calculated from water adsorption isotherms for the four samples.

	Ad-5	Ad-6	Ad-7	Ad-8
NH (%)	5.10	3.56	3.05	3.58
q_{ads} (mmol.g ⁻¹)	1.41	1.47	1.17	1.72
S (m ² .g ⁻¹)	90.2	93.6	74.8	109.5

However, the bentonite Ad-8 displayed the highest water adsorption across the entire range studied, owing to its elevated smectite content of saponite composition [59]. An analysis of the parameters derived from the water adsorption isotherms revealed a direct relationship between the natural humidity content (NH) of kerolite/stevensite clays and the proportion of stevensite present. NH values had a high correlation with S_{BET} , suggesting that water vapor adsorbs not only to the interlayer space but also to the mesoporous structure. The amount of water adsorption and the surface area calculated at 16.3% RH demonstrated that Mg-clays containing equivalent amounts of magnesian smectite (stevensite) exhibit similar characteristics.

Bentonite Ad-8 showed the highest total water adsorption, although its HN value was not the highest due to its swelling nature, which causes a significant portion of the total water to be interlayered (absorbed). Additionally, the monolayer surface areas of all materials correlated with the amount of smectite present: Ad-8 exhibited the highest

surface area, followed by Ad-5 and Ad-6 (both containing similar amounts of stevensite), with Ad-7 displaying the lowest.

This reverse order observed in the nitrogen adsorption–desorption isotherms indicates that while the presence of kerolite impacts the porous structure of the Mg-clays, it decreases their affinity for polar molecules such as water.

3.2. Adsorption Studies

The kinetic studies for both CPX and LID on Mg-clays are shown in Figure 7. The adsorption processes quickly achieved equilibrium removal at 120 min in all analyzed systems.

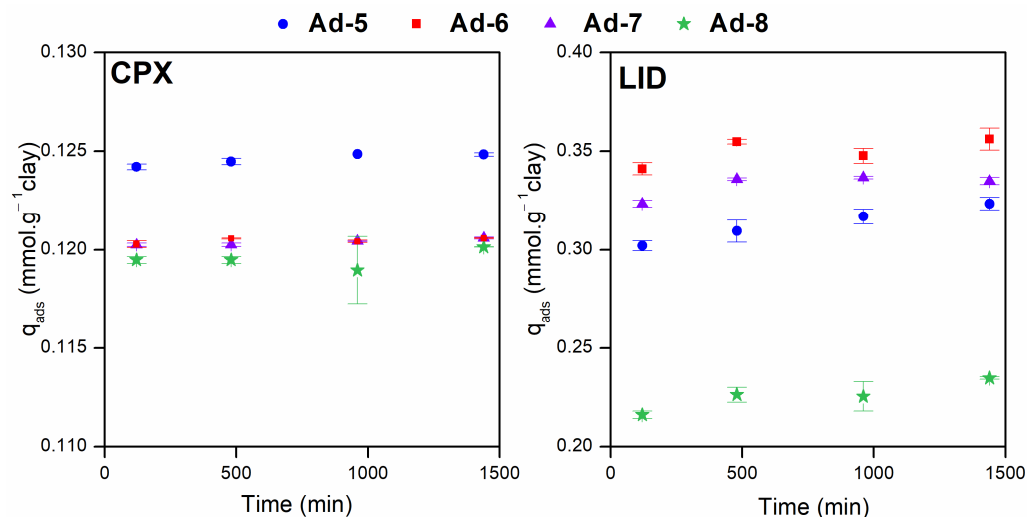


Figure 7. Kinetic studies for CPX and LID on Mg-clays at 20 °C.

The results showed that for CPX, the adsorbed amounts were similar in the four Mg-clays. Conversely, the amount of LID adsorption varied among the analyzed Mg-clays, the bentonite being the sample with the lowest values. This could suggest an influence of porous structure on LID molecule adsorption. This information indicated that all adsorption data obtained in this study can be considered obtained under equilibrium conditions.

In order to explain the adsorption results, it is important to consider that both CPX and LID are molecules with protonable groups and are pH-dependent in a solution [60,63]. In the studied conditions, the solutions were maintained at pH values close to 5, causing the predominant species of CPX to be the cationic form (CPX⁺), with a minor fraction existing as the zwitterion (CPX[±]), whereas for LID, the predominant species was its cationic form (LID⁺).

Figure 8 presents the experimental results and fitted isotherms for CPX and LID adsorbed on the Mg-clays. It was observed that CPX adsorption isotherms were L-type (Langmuir) for Ad-5 and H-type (high-affinity) for the other materials [73]. The L-type classification for Ad-5 suggests that the predominant species of CPX present in solution were adsorbed onto surface sites until saturation. On the other hand, H-type isotherms indicate that the predominant CPX species in solution exhibits a strong affinity toward the surface, evidenced by a much higher slope at initial concentrations. Both L- and H-type isotherms are associated with the adsorption of ionic solutes on materials and suggest that there is no significant competition among CPX species and the solvent for the available sites on the surface.

The Langmuir, Freundlich, and Sips isotherms were used to model the experimental data (Table 6). The Freundlich model correlated better with the experimental data of Ad-5 and Ad-7 samples, while the Sips model was the best fit for the experimental data of Ad-6 and Ad-8 samples. In any case, these models suggested that adsorption occurred in heterogeneous systems.

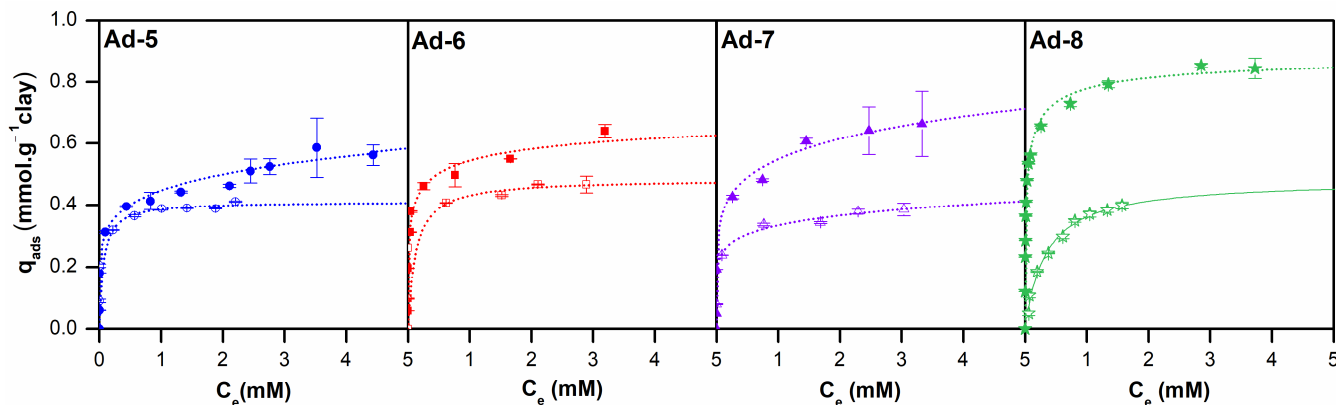


Figure 8. Adsorption isotherms of CPX (full points) and LID (empty points) at 20 °C on Mg-clays and their best fits.

Table 6. Langmuir, Freundlich, and Sips parameters for CPX and LID adsorption on Mg-clays.

		Ad-5		Ad-6		Ad-7		Ad-8	
		CPX	LID	CPX	LID	CPX	LID	CPX	LID
Langmuir	q_m (mmol g ⁻¹)	0.52	0.41	0.56	0.48	0.65	0.37	0.76	0.45
	k (L mmol ⁻¹)	13.5	16.4	47.9	8.22	11.9	19.3	75.4	3.00
	R^2	0.79	0.87	0.80	0.87	0.83	0.86	0.92	0.99
Freundlich	k_f (L g ⁻¹)	0.45	0.38	0.53	0.41	0.55	0.33	0.74	0.35
	n	6.34	6.92	6.18	5.93	6.11	7.63	6.01	2.34
	R^2	0.99	0.89	0.92	0.90	0.99	0.88	0.92	0.95
Sips	q_m (mmol g ⁻¹)	1.81	0.41	0.80	0.48	1.26	0.57	0.91	0.51
	b (L mmol ⁻¹) ^{1/n}	0.01	16.4	10.2	8.22	0.34	3.96	32.1	2.57
	n	4.39	1.00	3.01	1.00	4.07	3.40	1.95	1.09
	R^2	0.96	0.99	0.96	0.99	0.98	0.84	0.99	0.98

The Ad-8 bentonite exhibited the highest CPX-adsorption capacity, at 0.911 mmol·g⁻¹, equivalent to its CEC value (0.909 mmol·g⁻¹). In coherence with this, it also exhibited the highest smectite content of saponite composition, which may have favored CPX⁺ adsorption mainly through cationic exchange, which is the main adsorption mechanism reported for other smectite clay minerals [74].

For the kerolite/stevensite mixed layer, CPX adsorption was higher for Ad-6 than Ad-7, exhibiting adsorbed amounts exceeding their CEC values (Table 6). This would evidence that kerolite content favored CPX removal from the solution, which could be explained by two interrelated effects. As previously observed, kerolite/stevensite clays developed mesoporosity in their structure, potentially increasing the availability of surface sites such as broken edge sites for adsorbing the zwitterionic species of CPX in solution. The CPX[±] species presented a protonated amino group in its structure, while the carboxyl group was deprotonated, resulting in a neutral total charge that decreased its adsorption on the negative structure. The presence of the deprotonated carboxylate group could favor CPX interaction with the broken edge groups on the surface to form inner-sphere complexes, increasing the total amount adsorbed for these Mg-clays [39,52]. This was also observed by other authors in similar systems using pillared clays as adsorbents, which are characterized by a micro-mesoporous structure that favors CPX adsorption [30,50,51]. This suggests that in these non-swelling clay minerals, CPX could be adsorbed both as cation species on the negative charged surface and in zwitterion form on reactive sites located on the broken edge of the 2:1 structure. However, more specific determinations, such as the effect of pH and ionic strength on adsorption, are needed to elucidate the adsorption mechanisms of these clays.

Stevensite sample Ad-5 presented the lowest adsorption capacity. This could be explained by a much lower CEC than the bentonite Ad-8 and the absence of a kerolite phase that could have enhanced the adsorption, as explained above.

Adsorption isotherms for LID adsorption on Mg-clays were L-type (Langmuir) in Ad-5, Ad-6, and Ad-8 samples, while in the Ad-7 sample, these were H-type according to the classification proposed by Giles et al. [73]. Again, this would be evidence that ionic species adsorption, in this case, LID^+ , occurred without competing with water for the solid surface sites.

The adsorption parameters of Freundlich, Langmuir, and Sips models are presented in Table 6. The quadratic correlation values indicated in the good adjustment of samples Ad-5 and Ad-8 point to the Langmuir model and, in the case of Ad-6 and Ad-7, to the Freundlich model. These results suggest that in the Mg-clays with a higher smectite content, LID^+ adsorption took place in reactive sites of the same nature, while in the clays with kerolite content, adsorption occurred on reactive sites of a different nature.

The maximum adsorption capacity (q_m) for LID^+ on the analyzed clays, and therefore their removal efficiency, followed the order Ad-8 > Ad-6 > Ad-5 > Ad-7. Except for the bentonite Ad-8, the adsorbed amounts q_m obtained were equivalent to their CEC, suggesting that cation exchange is the main adsorption mechanism. In the case of the bentonite Ad-8 (97% saponite), the q_m value was lower than its CEC, suggesting that the LID molecule could occupy more than one available site in the saponite interlayer space, thus decreasing the number of sites. However, additional studies of Ad-8-LID adsorption complexes are needed in order to corroborate this.

All the samples showed a higher affinity and adsorption capacity for CPX than for LID in the studied conditions. This can be explained by considering the morphology and the size of the analyzed molecules as well as the Mg-clays properties. In the first place, CPX is a flat-shaped molecule with a lower thickness than LID. In addition, the positive charge of the CPX is located in its amine group situated at one end of the molecule, which would facilitate the interaction with the solids' surface. Meanwhile, in the LID molecule, voluminous carbon chains surround the protonated group, hindering interaction with the solid surface. Additionally, at the analyzed pH, the zwitterionic form of CPX is also present and therefore can be adsorbed on different surface reactive sites.

Taking all of this into account, bentonite Ad-8 exhibited the highest adsorption capacity for both CPX and LID under the studied conditions, which may be attributed to its higher smectite content of saponite composition and CEC value. This suggests that the primary mechanism of CPX and LID adsorption on the studied Mg-clays was cation exchange. This adsorption is likely facilitated by electrostatic forces between the positively charged CPX and LID molecules and the negative charge of the smectite component in the clays (saponite and stevensite).

However, in the case of CPX adsorption, the kerolite/stevensite mixed layer (Ad 6 and Ad-7) showed q_m values higher than their CEC values. In this case, the results suggested that CPX^\pm present could be adsorbed through another type of interaction, such as inner-sphere complexes or hydrogen bonds involving its deprotonated carboxyl group and -Si-OH or -Mg-OH groups exposed in broken edge sites. Such sites are associated with the porosity generated by the presence of kerolite in those samples, thereby increasing their adsorption capacity relative to their CEC values.

Finally, for a comparative performance assessment of the studied materials for CPX adsorption from aqueous media, the reported adsorption capacities for other natural clays are summarized and presented in Table 7. According to other authors, kaolinite clays feature the lowest adsorption capacities, followed by montmorillonite clay minerals (Na and Ca type). The studied Mg-clays in samples Ad-5 and Ad-7 presented values similar to montmorillonite types, but the values obtained in samples Ad-6 and Ad-8 surpassed them. This suggests that the composition of the mixed layer $\text{K}_{20}/\text{St}_{80}$ of Ad-6 adsorbed as much as a bentonite clay (Ad-8) with high purity (97% saponite).

Table 7. Adsorbed reports for CPX on natural clays.

Adsorbent	q _m CPX (pH) (mmol.g ⁻¹)	Adsorbent dosage (g.L ⁻¹)	Reference
kaolinite	0.02 (5–6)	0.2	[75]
Na-Bentonite from Turkey	0.44 (4.5)	2.5	[76]
Na-Montmorillonite from Argentine	0.42 (6)	2.5	[60]
Ca-bentonite	0.49 (6.5)	0.2	[12]
Clay 4 (Na-montmorillonite type)	0.58 (6–7.6)		
Clay 2 (Kaolin type)	0.09 (6–7.6)	1.0	[77]
Ad-5	0.44		
Ad-6	0.80	2.5	This work
Ad-7	0.55		
Ad-8	0.91		

The LID adsorption capacities were not included because no values have been previously reported for this molecule.

4. Conclusions

In this study, four Mg-clays were evaluated as potential adsorbents for the removal of two pharmaceutical pollutants: CPX and LID. Mineralogical analysis revealed that two of the clays are composed of a kerolite/stevensite mixed layer, the third is predominantly stevensite, and the fourth is classified as a bentonite with 97% saponite as its primary mineral component. Physicochemical characterization showed a strong correlation between the percentage of swelling clay minerals and the cation-exchange capacity (CEC) values. Textural properties indicated a significant influence of kerolite content, with a close relationship observed between the amount of kerolite and the percentage of mesoporosity.

Batch adsorption tests demonstrated that all materials are suitable for CPX and LID removal from water under the studied conditions. The results showed that for smectitic samples (saponite and stevensite), CPX adsorption primarily occurs through ionic exchange. Conversely, for samples containing kerolite, porosity plays a critical role by providing additional reactive sites within the porous structure and at the broken edges of clay particles. LID adsorption also appears to occur via ionic exchange, but due to the molecular shape of LID, this EC is more effectively accommodated in samples containing kerolite due to its higher pore volume.

This study not only underscores the potential of non-fibrous Mg-clays as adsorbents for emerging contaminants but also establishes a link between their composition, textural properties, and contaminant retention capacity. This understanding is essential for optimizing their application in various industrial contexts.

Author Contributions: Conceptualization: M.E.R.-J., M.P., T.M., M.T.B., G.P., L.V. and A.P.-A.; methodology: M.E.R.-J., V.R.-A., M.S. and A.M.; formal analysis: V.R.-A., M.S., A.M., M.E.R.-J., T.M., G.P. and M.P.; investigation: M.P., T.M., G.P., M.T.B. and M.E.R.-J.; resource: M.E.R.-J. and M.P.; data curation: V.R.-A., M.S., A.M., T.M., G.P. and M.P. writing—original draft preparation: M.E.R.-J., T.M. and M.P.; writing—review and editing: M.E.R.-J., T.M., M.T.B. and M.P.; project administration: M.E.R.-J. and M.P.; funding acquisition: M.P., L.V., M.T.B. and G.P. All authors have read and agreed to the published version of the manuscript.

Funding: This research was supported by the Autonomous University of Madrid (FUAM.2023/006) and the National University of Comahue (Argentina) under the auspices of Project I04-249, titled “Natural and Modified Clay Minerals for Applications in Health and Environment”, within the Faculty of Engineering.

Data Availability Statement: Data will be made available on request.

Acknowledgments: The authors gratefully acknowledge Minersa Group, the National University of Comahue (UNCo), PROBIEN-CONICET-UNCo, and the Autonomous University of Madrid for providing technology and financial support.

Conflicts of Interest: The authors declare no conflicts of interest.

References

1. Nikolenko, O.; Pujades, E.; Teixidó, M.; Sáez, C.; Jurado, A. Contaminants of emerging concern in the urban aquifers of Barcelona: Do they hamper the use of groundwater? *Chemosphere* **2023**, *341*, 140023. [[CrossRef](#)] [[PubMed](#)]
2. Gil, A.; Santamaría, L.; Korili, S.A.; Vicente, M.A.; Barbosa, L.V.; de Souza, S.D.; Marçal, L.; de Faria, E.H.; Ciuffi, K.J. A review of organic-inorganic hybrid clay based adsorbents for contaminants removal: Synthesis, perspectives and applications. *J. Environ. Chem. Eng.* **2021**, *9*, 105808. [[CrossRef](#)]
3. Gould, S.L.; Winter, M.J.; Norton, W.H.J.; Tyler, C.R. The potential for adverse effects in fish exposed to antidepressants in the aquatic environment. *Environ. Sci. Technol.* **2021**, *55*, 16299–16312. [[CrossRef](#)] [[PubMed](#)]
4. Reichert, G.; Hilgert, S.; Fuchs, S.; Azevedo, J.C.R. Emerging contaminants and antibiotic resistance in the different environmental matrices of Latin America. *Environ. Pollut.* **2019**, *255*, 113140. [[CrossRef](#)]
5. Kakakhel, M.A.; Nishita, N.; Navish, K.; Seyed Ali, J.; Syed Zaheer Ud, D.; Jiang, Z.; Khoo, K.S.; Shi, X. Deciphering the dysbiosis caused in the fish microbiota by emerging contaminants and its mitigation strategies—A review. *Environ. Res.* **2023**, *237*, 117002. [[CrossRef](#)]
6. Chaturvedi, P.; Shukla, P.; Giri, B.S.; Chowdhary, P.; Chandra, R.; Gupta, P.; Pandey, A. Prevalence and hazardous impact of pharmaceutical and personal care products and antibiotics in environment: A review on emerging contaminants. *Environ. Res.* **2021**, *194*, 110664. [[CrossRef](#)]
7. Lofrano, G.; Sacco, O.; Venditto, V.; Carotenuto, M.; Libralato, G.; Guida, M.; Meric, S.; Vaiano, V. Occurrence and potential risks of emerging contaminants in water. In *Visible Light Active Structured Photocatalysts for the Removal of Emerging Contaminants: Science and Engineering*; Elsevier: Amsterdam, The Netherlands, 2020; pp. 1–25.
8. Pulingam, T.; Parumasivam, T.; Gazzali, A.M.; Sulaiman, A.M.; Chee, J.Y.; Lakshmanan, M.; Chin, C.F.; Sudesh, K. Antimicrobial resistance: Prevalence, economic burden, mechanisms of resistance and strategies to overcome. *Eur. J. Pharm. Sci.* **2021**, *170*, 106103. [[CrossRef](#)]
9. Polianciuc, S.I.; Gurzău, A.E.; Kiss, B.; Georgia Ștefan, M.; Loghin, F. Antibiotics in the environment: Causes and consequences. *Med. Pharm. Rep.* **2020**, *93*, 231–240. [[CrossRef](#)]
10. Tran, N.H.; Hoang, L.; Nghiem, L.D.; Nguyen NM, H.; Ngo, H.H.; Guo, W.; Trinh, Q.T.; Mai, N.H.; Chen, H.; Nguyen, D.D.; et al. Occurrence and risk assessment of multiple classes of antibiotics in urban canals and lakes in Hanoi. *Vietnam. Sci. Total Environ.* **2019**, *692*, 157–174. [[CrossRef](#)]
11. Rúa-Gómez, P.C.; Püttmann, W. Impact of wastewater treatment plant discharge of lidocaine, tramadol, venlafaxine and their metabolites on the quality of surface waters and groundwater. *J. Environ. Monit.* **2012**, *14*, 1391–1399. [[CrossRef](#)]
12. Jara-Cobos, L.; Peñafiel, M.E.; Montero, C.; Menendez, M.; Pinos-Vélez, V. Ciprofloxacin Removal Using Pillared Clays. *Water* **2023**, *15*, 2056. [[CrossRef](#)]
13. Jara-Cobos, L.; Abad-Delgado, D.; Ponce-Montalvo, J.; Menendez, M.; Peñafiel, M.E. Removal of ciprofloxacin from an aqueous medium by adsorption on natural and hydrolyzed bentonites. *Front. Environ. Sci.* **2023**, *11*, 1239754. [[CrossRef](#)]
14. Igwegbe, C.A.; Oba, S.N.; Aniagor, C.O.; Adeniyi, A.G.; Ighalo, J.O. Adsorption of ciprofloxacin from water: A comprehensive review. *J. Ind. Eng. Chem.* **2021**, *93*, 57–77. [[CrossRef](#)]
15. Rúa-Gómez, P.C.; Püttmann, W. Occurrence and removal of lidocaine, tramadol, venlafaxine, and their metabolites in German wastewater treatment plants. *Environ. Sci. Pollut. Res.* **2012**, *19*, 689–699. [[CrossRef](#)] [[PubMed](#)]
16. Burch, K.D.; Han, B.; Pichtel, J.; Zubkov, T. Removal efficiency of commonly prescribed antibiotics via tertiary wastewater treatment. *Environ. Sci. Pollut. Res.* **2019**, *26*, 6301–6310. [[CrossRef](#)] [[PubMed](#)]
17. Ebrahimi, S.M.; Reyhani, R.D.; Asghari JafarAbadi, M.; Fathifar, Z. Diversity of antibiotics in hospital and municipal wastewaters and receiving water bodies and removal efficiency by treatment processes: A systematic review protocol. *Environ. Evid.* **2020**, *9*, 19. [[CrossRef](#)]
18. Sharma, S.; Bhattacharya, A. Drinking water contamination and treatment techniques. *Appl. Water Sci.* **2017**, *7*, 1043–1067. [[CrossRef](#)]
19. Bangia, S.; Bangia, R.; Daverey, A. Pharmaceutically active compounds in aqueous environment: Recent developments in their fate, occurrence and elimination for efficient water purification. *Environ. Monit. Assess.* **2023**, *195*, 1–27. [[CrossRef](#)]
20. Mangla, D.; Annu, Sharma, A.; Ikram, S. Critical review on adsorptive removal of antibiotics: Present situation, challenges and future perspective. *J. Hazard. Mater.* **2022**, *425*, 127946. [[CrossRef](#)]
21. Choudhry, A.; Sharma, A.; Khan, T.A.; Chaudhry, S.A. Flax seeds based magnetic hybrid nanocomposite: An advance and sustainable material for water cleansing. *J. Water Process Eng.* **2021**, *42*, 102150. [[CrossRef](#)]
22. Varsha, M.; Senthil Kumar, P.; Senthil Rathi, B. A review on recent trends in the removal of emerging contaminants from aquatic environment using low-cost adsorbents. *Chemosphere* **2022**, *287*, 132270. [[CrossRef](#)] [[PubMed](#)]
23. Barakan, S.; Aghazadeh, V. The advantages of clay mineral modification methods for enhancing adsorption efficiency in wastewater treatment: A review. *Environ. Sci. Pollut. Res.* **2021**, *28*, 2572–2599. [[CrossRef](#)] [[PubMed](#)]
24. França, D.B.; Trigueiro, P.; Silva Filho, E.C.; Fonseca, M.G.; Jaber, M. Monitoring diclofenac adsorption by organophilic alkylpyridinium bentonites. *Chemosphere* **2020**, *242*, 125109. [[CrossRef](#)] [[PubMed](#)]
25. Tharmavaram, M.; Pandey, G.; Rawtani, D. Surface modified halloysite nanotubes: A flexible interface for biological, environmental and catalytic applications. *Adv. Colloid. Interface Sci.* **2018**, *261*, 82–101. [[CrossRef](#)] [[PubMed](#)]

26. Zhao, B.; Liu, L.; Cheng, H. Rational design of kaolinite-based photocatalytic materials for environment decontamination. *Appl. Clay Sci.* **2021**, *208*, 106098. [[CrossRef](#)]
27. Song, N.; Hursthouse, A.; McLellan, I.; Wang, Z. Treatment of environmental contamination using sepiolite: Current approaches and future potential. *Environ. Geochem. Health* **2021**, *43*, 2679–2697. [[CrossRef](#)]
28. Rusmin, R.; Sarkar, B.; Biswas, B.; Churchman, J.; Liu, Y.; Naidu, R. Structural, electrokinetic and surface properties of activated palygorskite for environmental application. *Appl. Clay Sci.* **2016**, *134*, 95–102. [[CrossRef](#)]
29. Maged, A.; Kharbish, S.; Ismael, I.S.; Bhatnagar, A. Characterization of activated bentonite clay mineral and the mechanisms underlying its sorption for ciprofloxacin from aqueous solution. *Environ. Sci. Pollut. Res.* **2020**, *27*, 32980–32997. [[CrossRef](#)]
30. Maggio, A.A.; Roca-Jalil, M.E.; Villarroel-Rocha, J.; Sapag, K.; Baschini, M.T. Fe- and SiFe-pillared clays from a mineralogical waste as adsorbents of ciprofloxacin from water. *Appl. Clay Sci.* **2022**, *220*, 106458. [[CrossRef](#)]
31. Meziti, C.; Zaibet, W.; Benaidj, Y. Removal of ibuprofen from water using recycled clay waste. *Tob. Regul. Sci. (TRS)* **2023**, *9*, 4793–4804.
32. Akyuz, S.; Akyuz, T.; Akalin, E. Adsorption of isoniazid onto sepiolite-palygorskite group of clays: An IR study. *Spectrochim. Acta A Mol. Biomol. Spectrosc.* **2010**, *75*, 1304–1307. [[CrossRef](#)] [[PubMed](#)]
33. Cuevas, J.; Dirocie, N.; Yunta, F.; Delgado, C.G.; Santamaría DE, G.; Ruiz, A.I.; Fernández, R.; Eymar, E. Evaluation of the sorption potential of mineral materials using tetracycline as a model pollutant. *Minerals* **2019**, *9*, 453. [[CrossRef](#)]
34. Junior, H.B.; da Silva, E.; Saltarelli, M.; Crispim, D.; Nassar, E.J.; Trujillano, R.; Rives, V.; Vicente, M.A.; Gil, A.; Korili, S.A.; et al. Inorganic–organic hybrids based on sepiolite as efficient adsorbents of caffeine and glyphosate pollutants. *Appl. Surf. Sci. Adv.* **2020**, *1*, 100025. [[CrossRef](#)]
35. Li, Y.; Tian, G.; Gong, L.; Chen, B.; Kong, L.; Liang, J. Evaluation of natural sepiolite clay as adsorbents for aflatoxin B1: A comparative study. *J. Environ. Chem. Eng.* **2020**, *8*, 104052. [[CrossRef](#)]
36. Gómez-Avilés, A.; Sellaoui, L.; Badawi, M.; Bonilla-Petriciolet, A.; Bedia, J.; Belver, C. Simultaneous adsorption of acetaminophen, diclofenac and tetracycline by organo-sepiolite: Experiments and statistical physics modelling. *Chem. Eng. J.* **2021**, *404*, 126601. [[CrossRef](#)]
37. Davoud, B.; Mohadeseh, Z.; Shaziya, S. Investigation of Adsorptive Properties of Surfactant Modified Sepiolite for Removal of Ciprofloxacin. *Int. J. Life Sci. Pharma Res.* **2020**, *10*, 12–19.
38. Damacena DH, L.; Trigueiro, P.; Monteiro, V.H.; Honorio LM, C.; Duarte, T.M.; Cunha, R.; Furtini, M.B.; Fonseca, M.G.; da Silva-Filho, E.C.; Osajima, J.A. Saponite-inspired Materials as Remediation Technologies for Water Treatment: An Overview. *Environ. Process.* **2023**, *10*, 15. [[CrossRef](#)]
39. Antón-Herrero, R.; García-Delgado, C.; Alonso-Izquierdo, M.; García-Rodríguez, G.; Cuevas, J.; Eymar, E. Comparative adsorption of tetracyclines on biochars and stevensite: Looking for the most effective adsorbent. *Appl. Clay Sci.* **2018**, *160*, 162–172. [[CrossRef](#)]
40. De Vidales JL, M.; Pozo, M.; Alia, J.M.; Garcia-Navarro, F.; Rull, F. Kerolite-Stevensite mixed-layers from the Madrid basin, Central Spain. *Clay Miner.* **1991**, *26*, 329–342. [[CrossRef](#)]
41. Pozo, M.; Casas, J. Origin of kerolite and associated Mg clays in palustrine-lacustrine environments. The Esquivias deposit (Neogene Madrid Basin, Spain). *Clay Miner.* **1999**, *34*, 395–418. [[CrossRef](#)]
42. Temme, H.; Sohling, U.; Suck, K.; Ruf, F.; Niemeyer, B. Selective adsorption of aromatic ketones on kerolite clay for separation in biocatalytic applications. *Colloids Surf. A Physicochem. Eng. Asp.* **2011**, *377*, 290–296. [[CrossRef](#)]
43. Ulrich Sohling, F.; Haimeirl Agnes, H. Use of Stevensite for Mycotoxin Adsorption. U.S. Patent No. 8,221,807, 17 July 2012.
44. Ureña-Amate, M.D.; Socías-Viciano, M.; González-Pradas, E.; Saifi, M. Effects of ionic strength and temperature on adsorption of atrazine by a heat treated kerolite. *Chemosphere* **2005**, *59*, 69–74. [[CrossRef](#)] [[PubMed](#)]
45. Santarén, J. Properties and applications of magnesian clays. In *Magnesian Clays: Characterization, Origin and Applications*; Pozo, M., Galán, E., Eds.; AIPEA Educational Series; Pub. N° 2; Digilabs: Bari, Italy, 2015; pp. 123–174. ISBN 978-88-7522-093-8.
46. Ellass, K.; Laachach, A.; Alaoui, A.; Azzi, M. Removal of methyl violet from aqueous solution using a stevensite-rich clay from Morocco. *Appl. Clay Sci.* **2011**, *54*, 90–96. [[CrossRef](#)]
47. Fernández, R.; Ruiz, A.I.; García-Delgado, C.; González-Santamaría, D.E.; Antón-Herrero, R.; Yunta, F.; Poyo, C.; Hernández, A.; Eymar, E.; Cuevas, J. Stevensite-based geofilter for the retention of tetracycline from water. *Sci. Total Environ.* **2018**, *645*, 146–155. [[CrossRef](#)] [[PubMed](#)]
48. González-Pradas, E.; Socías-Viciano, M.; Saifi, M.; Ureña-Amate, M.D.; Flores-Céspedes, F.; Fernández-Pérez, M.; Villafrañca-Sánchez, M. Adsorption of atrazine from aqueous solution on heat treated kerolites. *Chemosphere* **2003**, *51*, 85–93. [[CrossRef](#)]
49. Socías-Viciano, M.M.; Tévar de Fez, J.; Ureña-Amate, M.D.; González-Pradas, E.; Fernández-Pérez, M.; Flores-Céspedes, F. Removal of chloridazon by natural and ammonium kerolite samples. *Appl. Surf. Sci.* **2006**, *252*, 6053–6057. [[CrossRef](#)]
50. Roca Jalil, M.E.; Baschini, M.; Sapag, K. Removal of ciprofloxacin from aqueous solutions using pillared clays. *Materials* **2017**, *10*, 1345. [[CrossRef](#)]
51. Roca Jalil, M.E.; Toschi, F.; Baschini, M.; Sapag, K. Silica pillared montmorillonites as possible adsorbents of antibiotics from water media. *Appl. Sci.* **2018**, *8*, 1403. [[CrossRef](#)]
52. Hu, Y.; Pan, C.; Zheng, X.; Liu, S.; Hu, F.; Xu, L.; Xu, G.; Peng, X. Removal of ciprofloxacin with aluminum-pillared kaolin sodium alginate beads (CA-Al-KABs): Kinetics, isotherms, and BBD model. *Water* **2020**, *12*, 905. [[CrossRef](#)]
53. Pozo, M.; Calvo, J.P. An overview of authigenic magnesian clays. *Minerals* **2018**, *8*, 520. [[CrossRef](#)]

54. Schultz, L.G. Quantitative Interpretation of Mineralogical Composition from X-ray and Chemical Data for the Pierre Shale. 1964. Available online: <https://pubs.usgs.gov/pp/0391c/report.pdf> (accessed on 6 August 2024).
55. Meier, L.P.; Kahr, G. Determination of the Cation Exchange Capacity (CEC) of Clay Minerals Using the Complexes of Copper (II) Ion with Triethylenetetramine and Tetraethylenepentamine. *Clays Clay Miner.* **1999**, *47*, 386–388. [[CrossRef](#)]
56. Villarroel-Rocha, J.; Barrera, D.; García Blanco, A.A.; Roca Jalil, M.E.; Sapag, K. Importance of the α -plot Method in the Characterization of Nanoporous Materials: Enhanced Reader. *Adsorpt. Sci. Technol.* **2013**, *31*, 165–183. [[CrossRef](#)]
57. Thommes, M.; Kaneko, K.; Neimark, A.V.; Olivier, J.P.; Rodriguez-Reinoso, F.; Rouquerol, J.; Sing, K.S.W. Physisorption of gases, with special reference to the evaluation of surface area and pore size distribution (IUPAC Technical Report). *Pure Appl. Chem.* **2015**, *87*, 1051–1069. [[CrossRef](#)]
58. Hatch, C.D.; Wiese, J.S.; Crane, C.C.; Harris, K.J.; Kloss, H.G.; Baltrusaitis, J. Water adsorption on clay minerals as a function of relative humidity: Application of BET and Freundlich adsorption models. *Langmuir* **2012**, *28*, 1790–1803. [[CrossRef](#)]
59. Akin, I.D.; Likos, W.J.; Asce, M. Evaluation of Isotherm Models for Water Vapor Sorption Behavior of Expansive Clays. *J. Perform. Constr. Facil.* **2017**, *31*, D4016001. [[CrossRef](#)]
60. Roca Jalil, M.E.; Baschini, M.; Sapag, K. Influence of pH and antibiotic solubility on the removal of ciprofloxacin from aqueous media using montmorillonite. *Appl. Clay Sci.* **2015**, *114*, 69–76. [[CrossRef](#)]
61. Mohammed, A.-O. Ciprofloxacin: Analytical Profile. *Profiles Drug Subst. Excip. Relat. Methodol.* **2004**, *31*, 179–207.
62. Powell, M.F. Lidocaine and lidocaine hydrochloride. *Anal. Profiles Drug Subst.* **1986**, *15*, 761–779.
63. Roca Jalil, M.E.; Sanchez, M.; Pozo, M.; Soria, C.O.; Vela, L.; Gurnik, N.; Baschini, M. Assessment of natural and enhanced peloids from the Copahue thermal system (Argentina): Effects of the drying procedure on lidocaine adsorption. *Appl. Clay Sci.* **2020**, *196*, 105751. [[CrossRef](#)]
64. Eberl, D.D.; Jones, B.F.; Khoury, H.N. Mixed-layer kerolite/stevensite from the Amargosa Desert, Nevada. *Clays Clay Miner.* **1982**, *30*, 321–326. [[CrossRef](#)]
65. Christidis, G.E.; Koutsopoulou, E. A simple approach to the identification of trioctahedral smectites by X-ray diffraction. *Clay Miner.* **2013**, *48*, 687–696. [[CrossRef](#)]
66. Madejová, J.; Gates, W.P.; Petit, S. IR Spectra of Clay Minerals. *Dev. Clay Sci.* **2017**, *8*, 107–149.
67. Guggenheim, S.; Koster van Groos, A.F. Baseline studies of the clay minerals society source clays: Thermal analysis. *Clays Clay Miner.* **2001**, *49*, 433–443. [[CrossRef](#)]
68. Sakizci, M.; Erdoğan Alver, B.; Alver, Ö.; Yörükoğullari, E. Spectroscopic and thermal studies of bentonites from Ünye, Turkey. *J. Mol. Struct.* **2010**, *969*, 187–191. [[CrossRef](#)]
69. Grim, R.; Rowland, R. Differential thermal analysis of clay minerals and other hydrous materials. Part 1. *Am. Mineral. J. Earth Planet. Mater.* **1942**, *27*, 746–761.
70. Grabowska-Olszewska, B.; Osipov, V.; Sokolov, V. *Atlas of the Microstructure of Clay Soils*; Panstwowe Wydawnictwo Naukowe: Varsovia, Poland, 1984.
71. El Mouzdahir, Y.; Elmchaouri, A.; Mahboub, R.; ElAnssari, A.; Gil, A.; Korili, S.A.; Vicente, M.A. Interaction of stevensite with Cd²⁺ and Pb²⁺ in aqueous dispersions. *Appl. Clay Sci.* **2007**, *35*, 47–58. [[CrossRef](#)]
72. González-Santamaría, D.E.; López, E.; Ruiz, A.; Fernández, R.; Ortega, A.; Cuevas, J. Adsorption of phenanthrene by stevensite and sepiolite. *Clay Miner.* **2017**, *52*, 341–350. [[CrossRef](#)]
73. Giles, C.H.; Smith, D. A General Treatment and Classification of the Solute Adsorption Isotherm. *J. Colloid. Interface Sci.* **1974**, *47*, 755–765. [[CrossRef](#)]
74. Lambert, J.F. Organic pollutant adsorption on clay minerals. *Dev. Clay Sci.* **2018**, *9*, 195–253.
75. Li, Z.; Hong, H.; Liao, L.; Ackley, C.J.; Schulz, L.A.; MacDonald, R.A.; Mihelich, A.L.; Emard, S.M. A mechanistic study of ciprofloxacin removal by kaolinite. *Colloids Surf. B Biointerfaces* **2011**, *88*, 339–344. [[CrossRef](#)] [[PubMed](#)]
76. Genç, N.; Dogan, E.C.; Yurtsever, M. Bentonite for ciprofloxacin removal from aqueous solution. *Water Sci. Technol.* **2013**, *68*, 848–855.
77. Gutiérrez-Sánchez, P.; Hrichi, A.; Garrido-Zoido, J.M.; Álvarez-Torrellas, S.; Larriba, M.; Victoria Gil, M.; Ben Amor, H.; García, J. Natural clays as adsorbents for the efficient removal of antibiotic ciprofloxacin from wastewaters: Experimental and theoretical studies using DFT method. *J. Ind. Eng. Chem.* **2024**, *134*, 137–151. [[CrossRef](#)]

Disclaimer/Publisher’s Note: The statements, opinions and data contained in all publications are solely those of the individual author(s) and contributor(s) and not of MDPI and/or the editor(s). MDPI and/or the editor(s) disclaim responsibility for any injury to people or property resulting from any ideas, methods, instructions or products referred to in the content.